Controlling the magnetic exchange coupling in hybrid heterojunctions via spacer layers of π-conjugated molecules

Quentin Arnoux,[1,2] Camille Blouzon,[3] Dongzhe Li,[3] Yannick J. Dappe,[3] Alexander Smogunov,[3] Pierre Bonville,[3] Ludovic Tortech,[1,2] and Jean-Baptiste Moussy[3]

[1]*NIMBE, CEA, CNRS, Université Paris-Saclay, CEA Saclay, Gif-sur-Yvette F-91191, France*

[2]*IPCM, Sorbonne Université, CNRS, Paris F-75005, France*

[3]*SPEC, CEA, CNRS, Université Paris-Saclay, CEA Saclay, Gif-sur-Yvette F-91191, France*

(Received 13 November 2018; revised manuscript received 25 February 2019; published 4 April 2019)

Mastering and understanding the magnetic couplings between magnetic electrodes separated by organic layers are crucial for developing new hybrid spintronic devices. We study the magnetic exchange interactions in organic-inorganic heterojunctions and unveil the possibility of controlling the strength of the magnetic exchange coupling between two ferromagnetic electrodes across π-conjugated molecules' (α-sexithiophene or para-sexiphenyl) ultrathin film. In Fe_3O_4/π-conjugated molecules/Co magnetic tunnel junctions, an antiferromagnetic interlayer exchange coupling with variable strength is observed according to the nature of the aromatic rings (thiophene or phenyl groups). The underlying physical mechanism is revealed by *ab initio* calculations relating the strength of magnetic coupling to the spin moment penetration into a molecular layer at the molecule/Co interface. The prospect that magnetic coupling between two ferromagnetic electrodes can be mediated and tuned by organic molecules opens different perspectives in the way magnetization of organic tunnel junctions or spin valves can be driven.

DOI: 10.1103/PhysRevB.99.144405

I. INTRODUCTION

Advances in the deposition of ultrathin metal films led to the new generation of devices with spin-dependent effects [1] and to the discovery of oscillatory magnetic coupling between ferromagnetic layers separated by a nonmagnetic spacer [2,3]. These magnetic heterostructures, also called spin valves, quickly found industrial applications due to their giant magnetoresistive properties. In order to further increase the performances of these devices, an extensive effort has been dedicated to develop tunnel magnetoresistive (TMR) heterostructures or magnetic tunnel junctions (MTJs). Several routes were investigated using ferromagnets with oxide tunnel barriers (e.g., Fe/MgO/Fe) [4], half metals (e.g., Fe_3O_4) to enhance TMR effects, or by fabricating all-semiconductor tunnel junctions. In parallel with these magnetotransport properties, unexpected interlayer exchange couplings (IECs) [5] have been observed such as antiferromagnetic coupling across insulating MgO [6] or semiconducting GaAs [7] layers. In all-metal heterostructures, the ferromagnetic (FM) or antiferromagnetic (AF) coupling can be explained by a Ruderman-Kittel-Kasuya-Yosida (RKKY)-type mechanism mediated by the nonmagnetic layer. Across insulating barriers, several models were proposed to account for IEC, either relying on the coupling of the evanescent part of surface states in free-electron models [8,9] or using tight-binding calculations [10]. However, such models cannot predict any significant coupling beyond 1 nm. Recent *ab initio* calculations [11] on $Fe_3O_4/vac/Fe_3O_4$ showed that IEC could turn into AF for barrier thicknesses $\sim 1-2$ nm and was strongly dependent on the interfacial oxygen-induced spin polarization. Impurity-assisted exchange coupling across a tunnel barrier, which is more suitable to reproduce the large IEC observed in MgO-based MTJs, has also been proposed [12]. Across organic thin layers, few studies have focused on this IEC effect [13]. Since the pioneering works concerning the integration of organic semiconductors as a spacer layer in hybrid heterostructures [14,15], a lot of studies have been dedicated to the spin injection into organic thin layers [16–19]. Hence, it is now well identified that the nature of the interface, also called spinterface [20–22], is crucial for the understanding of the transport properties. Peculiar magnetic properties have also been analyzed at the interface between organo-metallic molecules and a nonmagnetic or a FM metal surface [23–25]. However, only a few studies have been carried out on the magnetic behavior of complete hybrid heterostructures [26] and the understanding of the magnetic coupling between FM electrodes via organic molecules.

Here we report the use of organic molecules as a perspective for controlling and tuning the magnetic switching in organic-inorganic magnetic tunnel junctions. The magnetic exchange coupling taking place between magnetite (Fe_3O_4) and cobalt (Co) layers across organic monolayers (ML) of π-conjugated molecules (α-sexithiophene or para-sexiphenyl), represented in Fig. 1(a), is analyzed from an experimental and theoretical point of view. Depending on the number of organic layers, we show that it is possible to tune the strength of the magnetic exchange coupling in the heterojunction. In addition, we investigate the role of the chemical nature of the molecules (thiophene or phenylic units along the oligomeric chain) which allows the control of the physical mechanisms involved in the magnetic exchange couplings. Numerical simulations have been performed using density functional theory

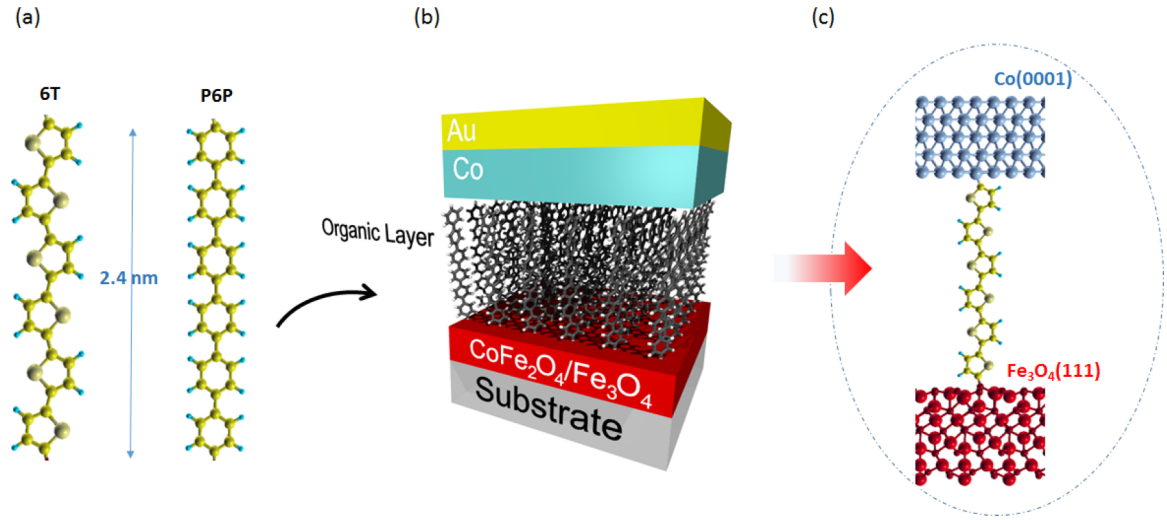

FIG. 1. Hybrid magnetic heterojunction with a π-conjugated molecules spacer layer. (a) Chemical structure of α-sexithiophene and para-sexiphenyl molecules. (b) Schematic illustration of the stack used for probing the magnetic exchange interactions. (c) Zoom of the chemical adsorption of organic molecules on an oxide surface.

(DFT) to support the results revealing the importance of molecular conjugation in the mechanism associated with the interlayer exchange coupling in the tunnel junction.

II. EXPERIMENT

Epitaxial ferrite thin films, $CoFe_2O_4$ and Fe_3O_4, were grown by oxygen-assisted molecular beam epitaxy (O-MBE) on crystalline a-Al_2O_3(0001) substrates. The O-MBE growth was performed using a radio-frequency oxygen plasma source and Knudsen effusion cells for Fe and Co evaporation. The oxygen partial pressure during deposition was 10^{-8} mbar. The Fe metallic deposition rate was 0.09 nm/min for Fe_3O_4. Co and Fe rates were set at 0.03 and 0.06 nm min^{-1}, respectively, in order to achieve a 1:2 Co to Fe ratio for $CoFe_2O_4$. High-purity 6T and P6P (TCI commercial product, purity = 99.99%) films were sublimated in another vacuum growth chamber (pressure in the high 10^{-7} mbar) on the Fe_3O_4(111) top layer as described previously for 6T-based heterojunctions [13]. For 6T (P6P), the growth was performed at a substrate temperature of 145 °C (180 °C) and an optimized rate of 0.1 nm min^{-1} (controlled with a quartz balance). With this method, molecules stand up on the surface from one single monolayer to an integer multiple of their lengths (estimated at 2.4 nm). The devices were completed by a slow rate deposition (below 0.4 nm min^{-1}) of Co electrode (8–10 nm) inside the same vacuum chamber to end up with Fe_3O_4/π-conjugated molecules/Co heterostructures. A 10 nm-thick Au capping layer was added in order to prevent oxidation of the Co counterelectrode.

Atomic force microscopy (AFM) images were recorded using a Pico-LE microscope (Molecular Imaging, Agilent Technologies) in contact mode in order to simultaneously probe the surface morphology and electrical properties. AFM tips were Si coated with Pt/Ir alloy with a stiffness between 0.1 and 0.3 N m^{-1}. The tip radius was given at 20 nm. The surface contact was estimated at 90 nm^2.

The chemical composition of the π-conjugated monolayers and Fe_3O_4/(6T or P6P) interfaces has been probed by x-ray photoemission spectroscopy (XPS) using a nonmonochromatized source with the Al Kα (1486.2 eV) or Mg Kα (1253.6 eV) radiation.

In-plane magnetic measurements on hybrid heterostructures were performed at various temperatures using a vibrating sample magnetometer (VSM) in a Quantum Design Physical Properties Measurement System (7 Tesla PPMS-VSM). Magnetic hysteresis loops were made from 300 to 10 K with an in-plane magnetic field of 2 Tesla during cooling. The diamagnetic contributions of the sample holder and substrate were removed in order to obtain the signal due solely to the magnetic deposited layers. The sensitivity in the magnetic moment is around 1 μemu at room temperature and the uncertainty on the applied magnetic field is $\pm$2 mT.

Analytical simulations of the hysteresis loops have been performed using a "steepest descent" minimization routine that determines the local minimum of the total energy of the coupled layers, which includes crystalline anisotropy and Zeeman terms together with an AF exchange coupling. This procedure assumes a coherent rotation of the magnetization [27]. We show that our model allows both major and minor experimental loops to be reproduced correctly and to derive the exchange bias integral. We furthermore investigate the peculiar properties of the loops in our case, where the ferrite bilayer has a strong anisotropy density and a weak magnetization, whereas the Co layer presents a weak anisotropy density and a high magnetization.

Atomic optimization and spin-polarized electronic structure calculations of the hybrid junctions have been performed using the *ab initio* plane-wave code QUANTUM ESPRESSO based on the density functional theory (DFT). The generalized gradient approximation in the Perdew-Burke-Ernzerhof (PBE) parametrization has been used for exchange-correlation functionals. Cutoffs of 30 and 300 Ry were employed for the wave functions and for the charge density, respectively. The van der Waals interactions were treated using semiempirical

dispersion corrections (DFT-D) in the Grimme's form as implemented in the QUANTUM ESPRESSO package.

III. RESULTS AND DISCUSSSION

A. Growth and structural analysis

Our stacks, illustrated in Fig. 1(b), consist of $CoFe_2O_4(5)/Fe_3O_4(20-30)/\pi$-conjugated molecules (x)/Co(9)/Au(8) layers (thicknesses are in nm) grown on sapphire substrates in ultrahigh vacuum conditions. The epitaxial ferrite thin films, $CoFe_2O_4$ and Fe_3O_4, were grown by O-MBE (see Fig. S1 in the Supplemental Material [28] for structural characterizations) according to the literature procedure [29]. The spinel oxide ($CoFe_2O_4$) is used as a buffer layer in order to increase the coercive field ($\mu_0 H_c$) of Fe_3O_4 from 0.03 Tesla to around 0.15-0.2 Tesla at 300 K (see Ref. [29] and Fig. S2 in the Supplemental Material [28] for magnetic details). The deposition of a Co counterelectrode on top of the organic layer results in an amorphous layer and, therefore, the magnetic reversal between this soft layer (coercive field around 3-5 mT at 300 K) and the hard Fe_3O_4 layer can be easily observed. Oligothiophene molecules such as α-sexithiophene (6T) and para-sexiphenyl (P6P) have been selected [Fig. 1(a)] as good candidates to form the organic layers because of their interest as an active material in devices such as light-emitting diodes or spintronics devices [30–32]. Moreover, both molecules are composed of aromatic core (see Fig. S3 in the Supplemental Material [28] for chemical formulas) and their length is less than 1% different. The π-conjugated molecules with a sufficient density are organized in a self-assembled monolayer whose properties are well known [33]. In particular, the molecules stand up perpendicularly to the surface, allowing the propagation of the magnetic polarization perpendicularly to the electrodes and along the molecular axis. In Fig. 1(c), we represent the extracted unit cell containing one molecule in the assembly used for the periodic *ab initio* calculations. Following experimental procedure, we assume that molecules are physisorbed on the Fe_3O_4 surface. Since their density is high enough, the molecular layer is self-assembled with molecular wires standing up on the Fe_3O_4. Upon further Co deposition, due to the kinetic energy of Co atoms, the hydrogen atoms at the extremity of the molecular wire are removed, involving a strong coupling of the Co atoms with the molecule. We assume therefore this situation of vertically stacked molecules, intact on the Fe_3O_4 side and making covalent C-Co bonds (with removed H atoms) on the other side. The unit cell of Fig. 1(c), periodically repeated in plane, was further adopted for our *ab initio* studies. Despite the presence of aromatic core in both molecules, the conjugation along the oligomer is highly different. Indeed, the 6T chain remains flat, allowing the delocalization of the electronic density. In contrast, for P6P, the steric hindrance due to the aromatic core (phenyl) imposed a twisted angle which breaks the conjugation between each phenyl core. 6T and P6P films were sublimated in another vacuum growth chamber on the $Fe_3O_4(111)$ top layer after an *in situ* cleaning of the oxide layer in order to avoid any surface contamination. The mastered growth of 6T and P6P thin films on Fe_3O_4 surfaces allowed one to obtain highly homogeneous and dense layers with thicknesses in the range $x = 0.5 - 4.0$ ML. The surface morphology of the organic layers has been checked by AFM (Fig. 2). The organic layers are grown from a nucleation center establishing a dense brush made of vertically aligned molecules on Fe_3O_4. As shown in Figs. 2(a) and 2(b), the deposition is perfectly controlled to reach thicknesses as low as $x = 1$ ML (i.e., 2.4 nm) either of P6P or of 6T (also see Fig. S4 in the Supplemental Material [28]). Once the growth of 1 ML is completed, the P6P and 6T films are continuous with a roughness of 0.3 nm root mean square (rms), equal to the underlying oxide. Right above the integer monolayer deposition (e.g., 2.1 ML), islands with a dendritic shape can be observed independently of the considered organic molecules [Figs. 2(c) and 2(d)]. The island height corresponds to an integer multiple of the P6P or 6T molecular length (around 2.4 nm). Consequently, the growth mode of both π-conjugated layers follows the same self-assembling rules, namely, a layer-by-layer growth, similar to the Franck–Van der Merwe model. Conductive AFM measurements have been performed on 6T and P6P monolayers. Figure 3 shows a typical resistance map of 1 ML of 6T at room temperature. The high resistances measured over extended areas confirm the lack of pinholes and the full coverage of the oxide surface by the organic monolayer. XPS spectra of the core levels (e.g., *S* 2*p*, *C* 1*s*) were recorded for the different Fe_3O_4/(6T or P6P) interfaces in order to probe the chemical composition of the π-conjugated molecular layers. The peak positions of the core levels (see Fig. S5 in the Supplemental Material [28] for the XPS analyses) are in good agreement with the expected values in 6T or P6P. The quantization of the peak intensities confirms the correct stoichiometry of the molecules within the accuracy limit of the XPS method ($\pm 15\%$). The heterojunction was completed by deposition of a Co counterelectrode in the same growth chamber as the organic layer, at room temperature, and at a slow evaporation rate. Finally, the stack was protected by a gold capping layer. X-ray reflectivity measurements confirmed the layer thicknesses and low interfacial roughnesses (see Fig. S6 in the Supplemental Material [28] for x-ray measurements on the heterojunction), which excludes surface degradation and major problems of interdiffusion from the top Co electrode.

B. Magnetic behavior in heterojunctions

In-plane magnetic hysteresis loops have been carried out for 6T and P6P ($x = 1$ and 2 ML) based heterojunctions. We measured both major and minor hysteresis loops.

Figure 4 presents the major loop at $T = 50$ K for the P6P (2 ML) heterojunction, which is typical for all our samples (except for the low-field magnetic behavior; see below). A major loop, where the field is swept from 3 Tesla to −3 Tesla and back, shows two jumps, possibly smeared, one at high field ($\mu_0 H_{c1}$), corresponding to the reversal of the hard ferrite magnetization, and one at low field ($\mu_0 H_{c2}$), corresponding to the reversal of the soft Co magnetization. At the scale of Fig. 4, the details of the hard ferrite reversal alone are visible, with a large domain of reversal fields ($0.5 < \mu_0 H_{c1} < 1$ T). This is due to the layer polycrystalline structure, inducing

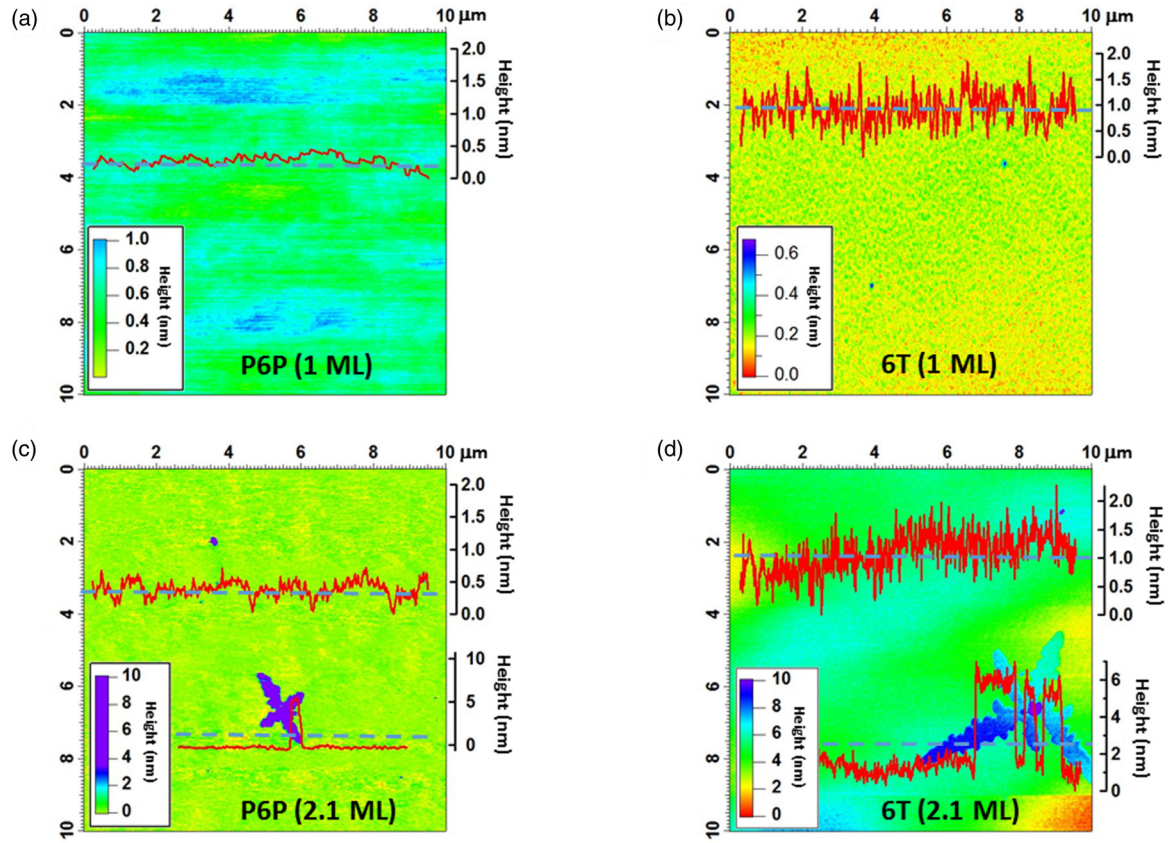

FIG. 2. AFM images of α-sexithiophene and para-sexiphenyl thin films. (a) AFM topography images (contact mode) of P6P (1 ML) and (b) 6T (1 ML) ultrathin films vacuum deposited on epitaxial $Fe_3O_4(111)$. Area: $10 \times 10\ \mu m^2$. (c) AFM topography images of P6P (2.1 ML) and (d) 6T (2.1 ML) thin films on $Fe_3O_4(111)$. Area: $10 \times 10\ \mu m^2$. The color-scale bars reflect the topography height. Inset line profiles correspond to the topography recorded along the dashed lines. The dendritic island with the associated profile line observed in (c) and (d) corresponds to an island (4 ML).

a random distribution of anisotropy axes, and also probably to its composite nature which implies a spread in the values of the anisotropy density. The reversal of the soft Co layer occurring at low field is also clearly visible. This magnetic hysteresis loop allows one to confirm that no notable diffusion of Co into the organic layer is present. If interdiffusion and/or degradation of the interface was dominant, the magnetic behavior of the heterojunction would be that of one single layer. The simulations to be presented below reproduce quite well the overall shape of the major hysteresis loop and yield values of the switching fields and magnetization height ratios in good agreement with the film thicknesses and standard magnetizations, proving that the magnetic property of each FM layer is maintained.

Observation of the detail of the soft Co layer reversal needs to examine the major loop near zero field, and differences in behavior between samples appear by performing minor hysteresis loops. In a minor loop, the field is swept from 3 Tesla to −400 mT (i.e., before the hard layer magnetization is reversed) and back, and it shows only one jump corresponding to the reversal of the soft Co magnetization. Figure 5 shows close-ups near zero field of the loops for the 6T (2 ML) and P6P (2 ML) based heterojunctions at $T = 50$ K. Independently of the type of molecule, these curves show similar features. The major loops [Figs. 5(a) and 5(c)] evidence a reversal field ($\mu_0 H_{c2}$) of the soft Co layer near $\pm 15 - 20$ mT. This is a standard behavior for noninteracting magnetic layers. However, the minor loops [Figs. 5(b) and 5(d)], in some samples, are slightly shifted towards positive fields, i.e., showing a small positive exchange bias field ($\mu_0 H_{ex}$) around $5 - 10$ mT. It has been shown that this behavior indicates the presence of an AF coupling [34] between layers.

Figure 6 shows close-ups of the loops for the 6T (1 ML) and P6P (1 ML) based MTJs. As we previously observed in Ref. [13], for the 6T (1 ML) based MTJ, the loops are strikingly different from those with 2 ML. The major loop shows a crossing of the two branches [Fig. 6(a)], the reversal field of the soft layer being shifted to negative fields, and the remanence being close to zero. As to the minor loop [Fig. 6(b)], it shows a rather high exchange bias field ($\mu_0 H_{ex} \approx 100$ mT), together with an upwards flaring. The opposite effect of AF exchange on the soft layer reversal field in major and minor loops is easy to explain (considering, for instance, the "return" branch): at that point, in a major loop, the hard layer magnetization is parallel to the soft layer one, both being opposite to the applied field, so the AF exchange

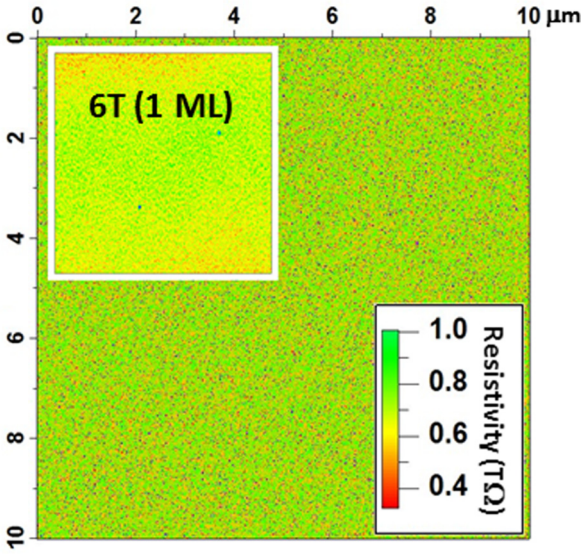

FIG. 3. Resistance map of 6T (1 ML) deposited onto a $Fe_3O_4(111)$ thin film recorded by current-sensing AFM at a tip voltage of 500 mV with the associated AFM topography in the inset. This image reveals a highly homogeneous and insulating behavior with resistances ranging from 500 GΩ to 1 TΩ.

field on the soft layer is opposite to its magnetization and parallel to the applied field, and thus helps the reversal which can take place at a lower applied field. The situation is the reverse in a minor loop, where the hard layer magnetization is not reversed at that point, and hence the exchange field hinders the soft layer reversal, resulting in a positive shift of the loop.

On the other hand, the loops for P6P (1 ML) based MTJs [Figs. 6(c) and 6(d)] are similar to those for P6P (2 ML). Thus, while the AF coupling is practically destroyed for both the 2 ML based heterojunctions and for the P6P (1 ML) based heterojunction, with a bias field of 5–10 mT, it is quite strong

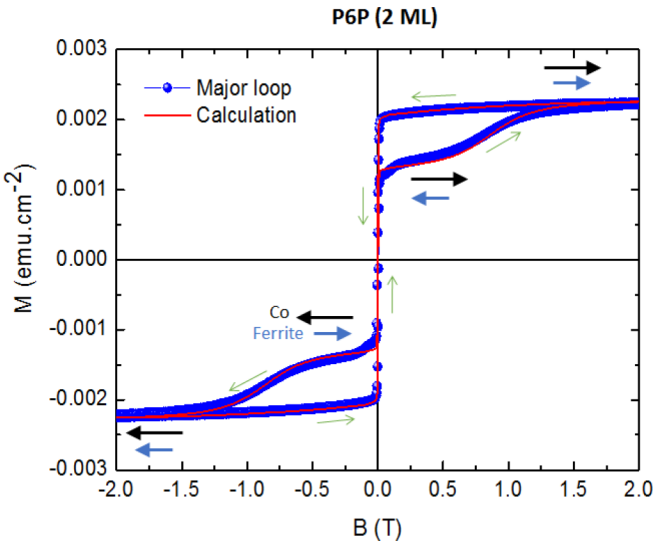

FIG. 4. Major hysteresis loop at $T = 50$ K for the P6P (2 ML) based heterojunction. The solid line is a calculation using the model described in the text.

in the 6T (1 ML) based MTJ, where the bias field is around 100 mT, i.e., one order of magnitude larger. A similar behavior of the major loops in the presence of AF exchange has been observed in an oxide-based superlattice, but it was attributed to a different mechanism [35].

C. Analytical simulations of hysteresis loops

In order to model these hysteresis loops and to retrieve the relevant parameters, we simulate the magnetic behavior of the MTJs by two macrospins with magnetization M_1 and M_2 associated to the ferrite and Co layers, respectively ($M_1 < M_2$), coupled by an interfacial AF exchange coupling (J_{AF}). One must also take into account the crystalline anisotropy in the two layers. Since the hard ferrite bilayer is polycrystalline, we assume that the anisotropy in each crystallite is of the axial type, with density K_1, and that its axis is distributed at random, with angle ϕ, with respect to the magnetic field direction. Since it is dual (Fe_3O_4 and $CoFe_2O_4$), we also assume a small Gaussian distribution of the K_1 values. As to the soft amorphous Co layer with large magnetization, we assume that its anisotropy axis is parallel to the field and we take a unique value K_2 for its anisotropy density ($K_2 < K_1$). We also assume a small distribution of J_{AF} values. With these approximations, i.e., using the three distributed parameters K_1, ϕ, and J_{AF}, the calculations of the loops can be performed within a reasonable computer time. We have checked on a few examples in which introducing an extra distribution of K_2 values or axis orientations does not improve the agreement with experiment. Thus, the total energy (E) of the MTJ, including exchange, crystalline anisotropy, and Zeeman terms, is written, assuming in-plane magnetization for the two layers,

$$E = [K_1 \sin^2(\theta_1 - \phi) - \mu_o \mathrm{H} \mathrm{M}_1 \cos\theta_1]\mathrm{t}_1 + [\mathrm{K}_2 \sin^2\theta_2 - \mu_0 \mathrm{H} \mathrm{M}_2 \cos\theta_2]\mathrm{t}_2 + J_{\mathrm{AF}} \cos(\theta_2 - \theta_1),$$

where $\theta_1(\theta_2)$ is the deviation angle of $\mathbf{M}_1(\mathbf{M_2})$ from the direction of the applied field ($\mu_0 H$), ϕ is the angle of the anisotropy axis of a crystallite in the ferrite bilayer with respect to the field, and $t_1(t_2)$ is the thickness of layer 1 (2). The exchange integral J_{AF} is taken positive for AF coupling. For each value of ϕ, the energy is minimized with respect to θ_1 and θ_2 and, after integration, the total in-plane magnetization (m) is obtained as

$$\mathrm{m} = \mathrm{M}_1 \mathrm{t}_1 \cos\theta_1 + \mathrm{M}_2 \mathrm{t}_2 \cos\theta_2$$

The simulation of the major loop for P6P (2 ML) (solid line in Fig. 4) allows one to determine, for the hard ferrite layer, $K_1 = 1.4 \times 10^5$ J/m^3 and the rms deviation $\Delta K_1 = 0.3 \times 10^5$ J/m^3, and the magnetization $M_1 = 180$ kA/m, and, for the soft Co layer, $M_2 = 1550$ kA/m, using thicknesses $t_1 = 27.5$ nm and $t_2 = 9$ nm. These values are typical for these materials, and the distributions in orientation and values for the anisotropy of the hard layer reproduce well the large range of its reversal fields. For the 6T and P6P (1 ML) loops of Fig. 6, the simulations correctly reproduce the details of the major and minor hysteresis loops, in particular the almost tangential crossing of the major loop branches in 6T (1 ML). The thicknesses for the 6T (1 ML) sample are the same, but $t_2 = 14$ nm for the P6P (1 ML) based MTJ. We

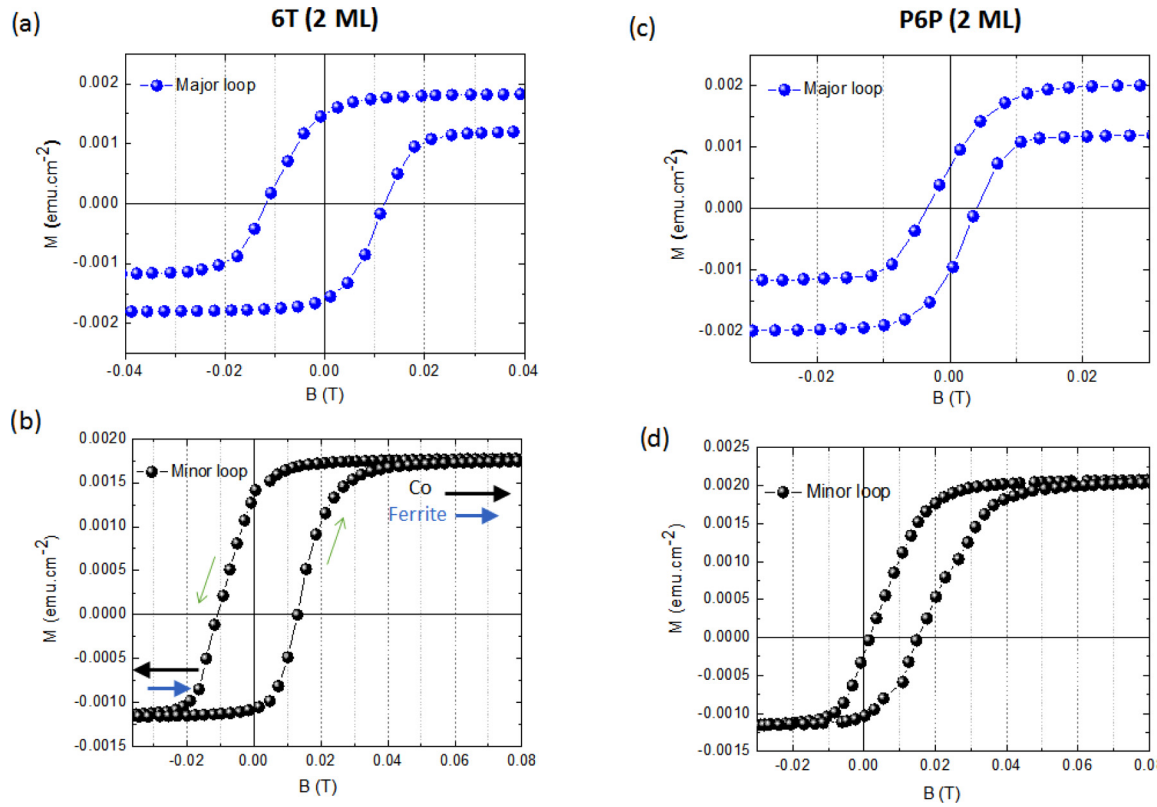

FIG. 5. Major and minor hysteresis loops near zero field at $T = 50$ K for the (a),(b) 6T (2 ML) based heterojunction and the (c),(d) P6P (2 ML) based heterojunction. Both minor loops show a small positive exchange field around 5–10 mT.

obtain somewhat different parameter values, still in the correct range for these materials: $K_1 = 3.8 \times 10^5\,\mathrm{J/m^3}$, $\Delta K_1 = 0.4 \times 10^5\,\mathrm{J/m^3}$, and $M_1 = 400\,\mathrm{kA/m}$, $M_2 = 1350\,\mathrm{kA/m}$. These discrepancies can probably be attributed to details in the manufacturing process of the samples. We can further determine $K_2 = 8 \times 10^4\,\mathrm{J/m^3}$, and the exchange coupling, which is found to be rather large, $J_{AF} = 11.5 \times 10^{-4}\mathrm{J/m^2}$ ($\Delta J_{AF} = 3.8 \times 10^{-4}\,\mathrm{J/m^2}$) for 6T (1 ML), whereas it is smaller, $J_{AF} = 2.0 \times 10^{-4}\,\mathrm{J/m^2}$ ($\Delta J_{AF} = 0.5 \times 10^{-4}\,\mathrm{J/m^2}$) for P6P (1 ML). In the frame of this model, the exchange field is linked to the exchange integral by the relation (see Ref. [34]) $\mu_0 H_{ex} = J_{AF}/(t_2 M_2)$. Using the above determined values, we find $\mu_0 H_{ex} = 100\,\mathrm{mT}$ for 6T (1 ML) and 10 mT for P6P (1 ML). This corresponds well to what can be directly read on the experimental curves, giving thus confidence that our model, though simplified, correctly reflects the physics of these MTJs.

As discussed above, an AF coupling between bilayers is characterized by a positive exchange field for the minor loop, but our simulations also reproduce a peculiar upwards flaring of this loop [Fig. 6(b)]. The stronger the exchange coupling, the more pronounced the flaring. For the weak AF exchange coupling present for P6P (1 ML) [Fig. 6(d)], this flaring has practically vanished. In Fig. 7(a), we have compared simulated minor loops for two opposite values of the exchange: for FM coupling, the flaring is also present, but it is downwards. In Fig. 7(b), we show simulations of the major loop near zero field for increasing values of the exchange integral J_{AF}, to exemplify the crossover. The other parameter values are close to those determined experimentally, but somehow changed for the effect to be more visible. For $J_{ex} = 4 \times 10^{-4}\,\mathrm{J/m^2}$, the loop is standard, i.e., the branches do not cross; for $J_{ex} = 6 \times 10^{-4}\,\mathrm{J/m^2}$, the two branches cross; and they are tangent for $J_{ex} = 4.75 \times 10^{-4}\,\mathrm{J/m^2}$.

D. *Ab initio* calculations

To understand the physical mechanism underlying the magnetic behavior of the MTJs, atomic optimization and spin-polarized electronic structure calculations have been performed on the unit cell represented in Fig. 1(c) using *ab initio* plane-wave code based on DFT. The van der Waals interactions were treated using semiempirical dispersion corrections (DFT-D). Unfortunately, due to significant lattice mismatch between Fe_3O_4 and Co (about 15%), the straightforward calculation of full Fe_3O_4/π-conjugated molecules/Co systems is problematic from a computational point of view (since the same in-plane periodicity of a supercell is required in DFT calculations), so we have rather chosen to separately analyze the molecular interfaces with two magnetic surfaces. That will provide, moreover, a much deeper understanding of interfacial effects and of the mechanism behind magnetic coupling mediated by organic spacers.

We start with a Co/molecule interface (Fig. 8) since molecules are expected to bind much stronger (structurally and magnetically) to the cobalt as suggested by experimental conditions. We first discuss the 6T molecule [Fig. 8 (a)]. The cobalt was simulated for simplicity by a five-layer hexagonal compact slab to which the molecule binds by an extreme carbon atom (a hydrogen atom is supposed to be expelled

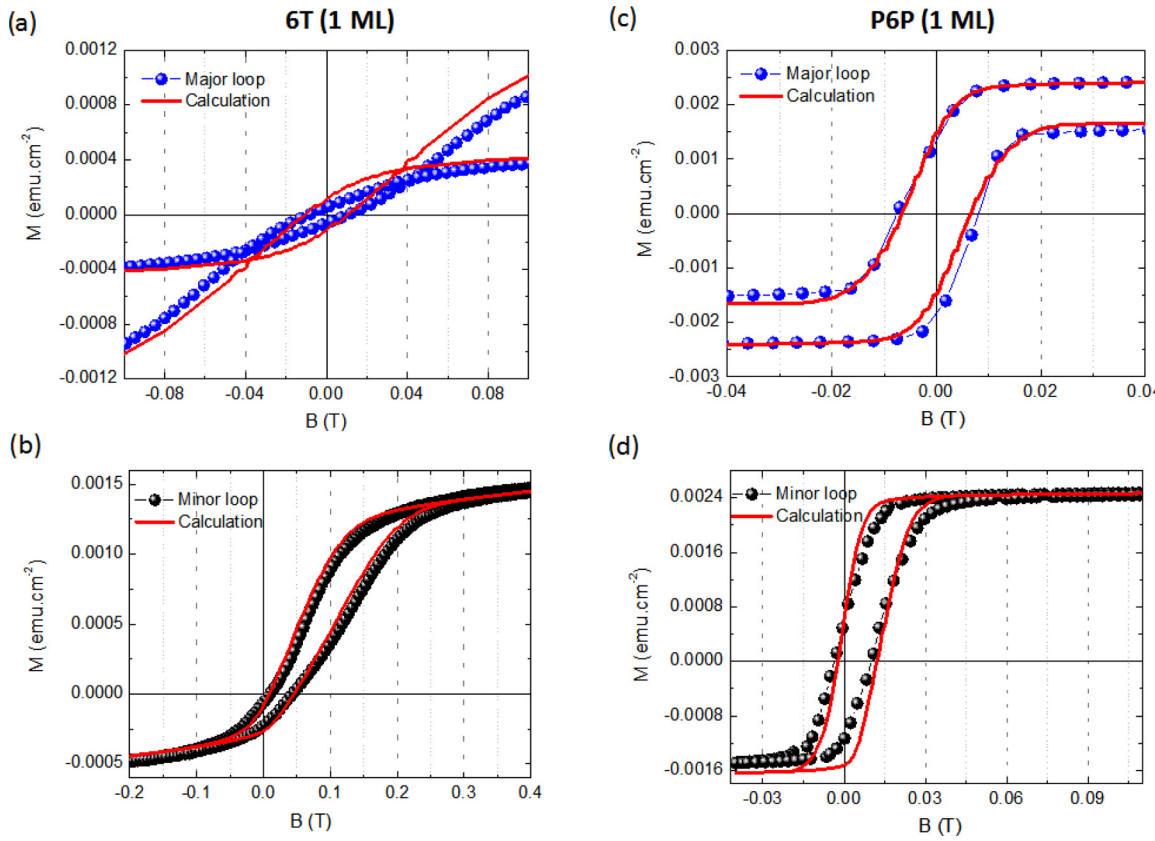

FIG. 6. Major and minor hysteresis loops near zero field at $T = 50$ K for the (a),(b) 6T (1 ML) based heterojunction and the (c),(d) P6P (1 ML) based heterojunction. The solid lines are calculations using the model described in the text. For 6T (1 ML), (a) the major loop exhibits a crossover near zero field and (b) the minor loop shows a sizeable positive exchange, with a large exchange field of about 100 mT, together with an upwards flaring. For P6P (1 ML), (c) no crossover of the major loop is observed and (d) the minor loop exhibits a small exchange field of ≈10 mT.

by the arriving hot Co atoms). A bridge adsorption position was found to be energetically preferable, as shown in the upper panel of Fig. 8(a). The magnetic moment of the Co slab was found to propagate over the molecule due to the proximity effect, as shown in the middle panel of Fig. 8(a). It is mainly distributed on the carbon atoms, showing oscillating behavior and decaying further from the Co slab. This induced molecule spin moment is then responsible for the magnetic coupling between Co and Fe_3O_4 electrodes if a Fe_3O_4 surface is attached on the right side. Interestingly, the spin moment always presents the same (positive) sign on the last atom of each monomer, which suggests that the magnetic coupling is also of the same sign (AF or FM) for the *n*-thiophene molecules of different lengths, decaying monotonically with the number n of monomers. The decay rate of the induced Co spin moment may depend on the nature of the molecule. This exhibits the possibility to manipulate the induced spin moment (sign, propagation distance) and thus the magnetic exchange coupling in the hybrid heterostructure via the choice of the molecules. To confirm this idea, DFT calculations have been performed by replacing the thiophene groups by phenyl groups defining the P6P molecule. Substituting the thiophene group by phenyl does not change the organic spacer length [see Fig. 1(a)] in the MTJ, but we expect to modulate the electronic transport along the chains by changing the chemical nature of the π-conjugated molecule. Indeed, 6T is flat, which induces a conjugation along the chain, while in P6P, due to the steric effect, each phenyl unit is twisted (without $3p_z$ orbitals overlapping), leading to a poor conjugation. Hence, each phenyl unit can be considered as independent in P6P, which could break the electronic propagation and could be responsible for a different magnetic interaction, as measured in Fig. 6. These DFT calculations clearly reveal [Figs. 8(b) and 8(c)] this assessment. Figure 8(b) shows a model of a flat para-sexiphenyl molecule. It can indeed be seen that the decay of the spin moment is much smaller in this case compared to the sexithiophene. We can correlate such a difference to the position of the highest occupied molecular orbital (HOMO). This orbital was found to be much closer to the Fermi level for the sexithiophene molecule, as illustrated in the lower panels of Fig. 8(b), where the molecular density of states (DOS) is presented. We argue, thus, that the closer the HOMO is to the Fermi level, the longer is the spin moment propagation across the molecule due to a smaller wave-function decay rate at the Fermi energy. This argument, related to the electronic tunneling barrier at the interface, is also used in electronic transport when discussing the attenuation of conductance in molecular junctions [32,36]. Note that here we consider the HOMOs rather than the lowest unoccupied molecular orbitals (LUMOs) since the latter, much farther from the Fermi level,

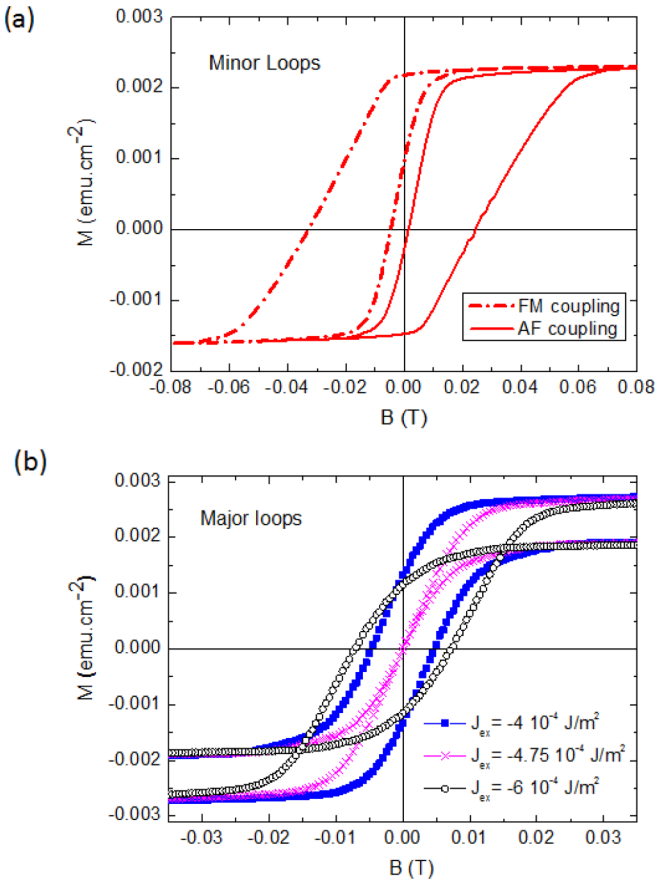

FIG. 7. Simulations of magnetic hysteresis loops: (a) minor loops for bilayers with AF and FM coupling, for $|J_{ex}| = 5 \times 10^{-4}\,\mathrm{J/m^2}$, showing the opposite flarings for the two cases; (b) major loops for AF coupled bilayers for increasing values of the exchange coupling. At $J_{ex} = 4 \times 10^{-4}\,\mathrm{J/m^2}$, the branches do not cross; at $J_{ex} = 4.75 \times 10^{-4}\,\mathrm{J/m^2}$, the branches cross tangentially; and at $J_{ex} = 6 \times 10^{-4}\,\mathrm{J/m^2}$, the two branches cross.

are not relevant in the present case. For realistic twisted para-sexiphenyl molecules, presented in Fig. 8(c), when the consecutive monomers are randomly rotated in a range from 15° to 30°, a further suppression of the spin moment propagation is effectively observed. This additional effect is not directly related to the wave-function decay discussed above—since the HOMOs levels are almost at the same positions for both flat and twisted molecules—but rather to an additional breaking of conjugations along the molecule. We can thus summarize that two factors lead to the decrease of the spin moment propagation in P6P with respect to 6T: (i) electronic (faster wave-function decay due to a more distant HOMO level from the Fermi energy) and (ii) structural (breaking of the conjugation along the molecular chain). Therefore, the very strong spin moment decay in P6P results in a negligible magnetic coupling in Fe_3O_4/P6P/Co, or at least much weaker than in Fe_3O_4/6T/Co as observed experimentally.

In order to get insight into the sign of the magnetic coupling between Co and Fe_3O_4 electrodes mediated by the two examples of molecules discussed above, we have performed similar calculations for molecule/Fe_3O_4 interfaces. Among many possible (and appearing statistically in experiment) surfaces terminations of $Fe_3O_4(111)$ [37], we have considered two possibilities: termination by octahedral (octa) Fe and by tetrahedral (tetra) Fe layers, as shown in Figs. 9(a) and 9(b), respectively. These terminations were chosen as representative since they display opposite magnetizations at the surface, as can be seen on the insets due to positive (negative) spin moments located on octa (tetra) Fe atoms. Contrary to the Co/molecule case, we kept the molecules intact (with an *H* pointing to the surface; upper panels of Fig. 9) which corresponds to the gentle deposition process realized experimentally. The molecules therefore bind rather weakly (physisorption) to the Fe_3O_4 slabs with an H-Fe_3O_4 distance of about 0.22 nm as found in our DFT calculations. For both terminations, we find that molecules tend to acquire a small negative magnetic moment, opposite to the overall positive moment of Fe_3O_4, leading to a gain in total energy. Similarly to the case of Co, the induced spin moment is much weaker for the P6P molecule compared to the 6T one. We therefore deduce that the molecules choose an AF magnetic alignment with respect to the Fe_3O_4 slab. From another side, as has been discussed above for Co/molecule interfaces, the induced Co spin moment is always positive (FM with respect to the Co slab) at the molecule extremity which points to the Fe_3O_4 slab (Fig. 8, middle panels). As predicted by our calculations, the coupling between the Co and Fe_3O_4 slabs is AF, which is in agreement with our experimental findings. This AF coupling should occur for all lengths of *n*-thiophene molecules, while it is predicted to be vanishingly small for the *n*-phenyl molecules due to very short spin moment propagation discussed above [Fig. 8(c)]. Note that DFT formalism is known in general to have problems in describing the exact alignment of molecular levels with respect to the Fermi energy imposed by metallic surfaces and, in particular, molecular HOMO-LUMO gap. However, we believe that this systematic error does not affect the physical trend and differences between two molecular systems. One can also argue that more accurate treatments of molecular orbitals (such as the GW approach, for example) may be needed if interested in a correct HOMO-LUMO gap. However, it has been shown that GW corrections affect rather unoccupied orbitals (poorly described within the ground-state DFT), while occupied levels (in particular, the HOMO) are only slightly altered [38]. Since in our case the magnetic coupling is controlled by the HOMO orbital, we believe that ordinary DFT results are enough to provide reliable comparative results.

IV. CONCLUSION

In summary, the growth of π-conjugated molecules (6T and P6P) in thin films ($0.5 < x < 4$ ML) has been performed on crystalline $Fe_3O_4(111)$ surfaces. AFM microscopy revealed the structural homogeneity and continuity of the 6T and P6P layers with low roughness down to 1 ML (i.e., 2.4 nm). A combined magnetic analysis and *ab initio* calculations have shown that the magnetic coupling between Fe_3O_4 and Co magnetic electrodes is highly dependent on the organic thickness and on the choice of the π-conjugated molecule. A clear AF coupling is observed in Fe_3O_4/π-conjugated molecules/Co magnetic tunnel junctions for 6T ($x = 1$ ML), while this exchange coupling is much smaller for

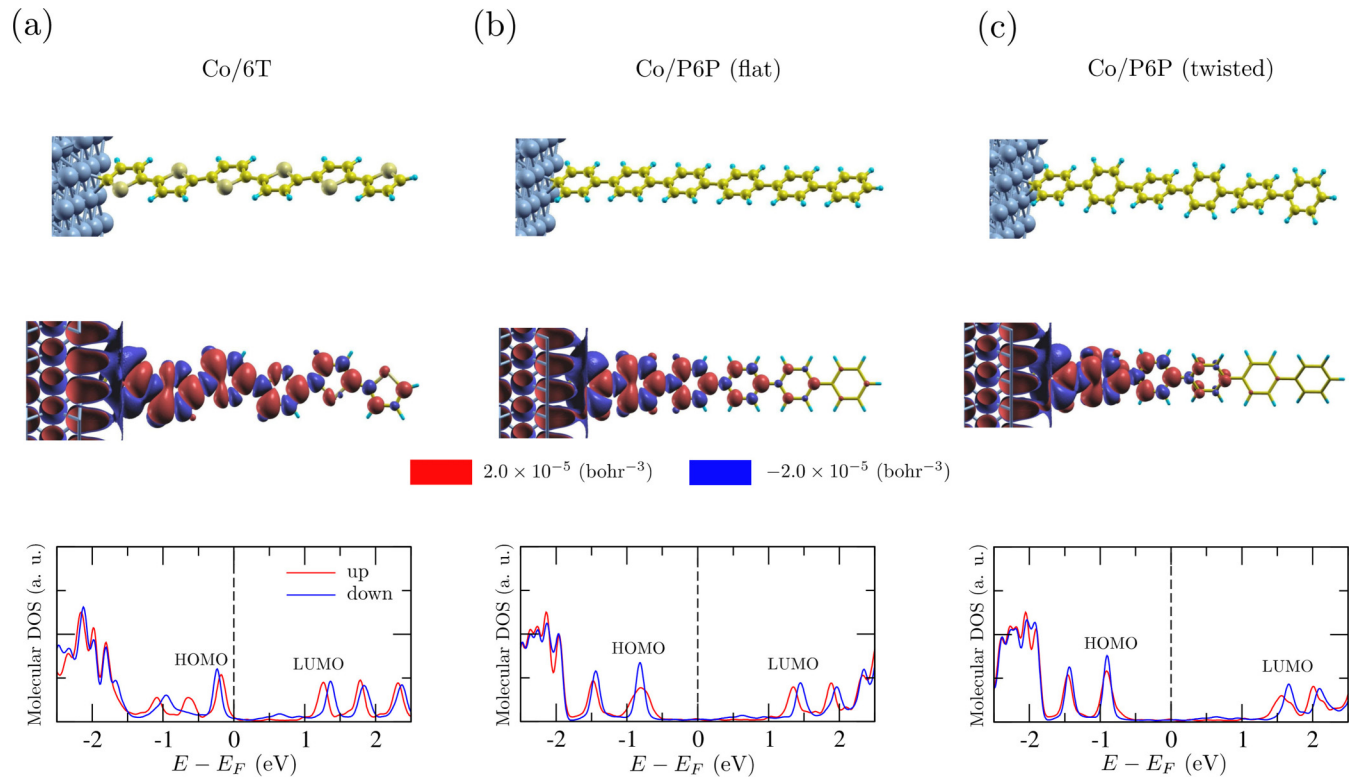

FIG. 8. DFT results for hybrid Co/π-conjugated molecule interfaces. (a) Co/6T interface. (b) Co/P6P interface with a molecule in a model with flat configuration. (c) Co/P6P interface with a molecule in a realistic twisted configuration. Upper panels: Co/molecule adsorption configuration. Middle panels: three-dimensional plots of spin magnetization for positive (red) and negative (blue) isovalues. Lower panels: DOS projected onto all molecular orbitals; the HOMO and LUMO molecular orbitals are marked.

P6P ($x = 1$ ML). DFT calculations showed that the substitution of thiophene by phenylic units along the oligomeric chain hinders the induced magnetic moment propagation across the P6P molecule in comparison with the 6T molecule. Two effects, electronic and geometric, were identified to stay at the origin of much smaller spin moment propagation for P6P

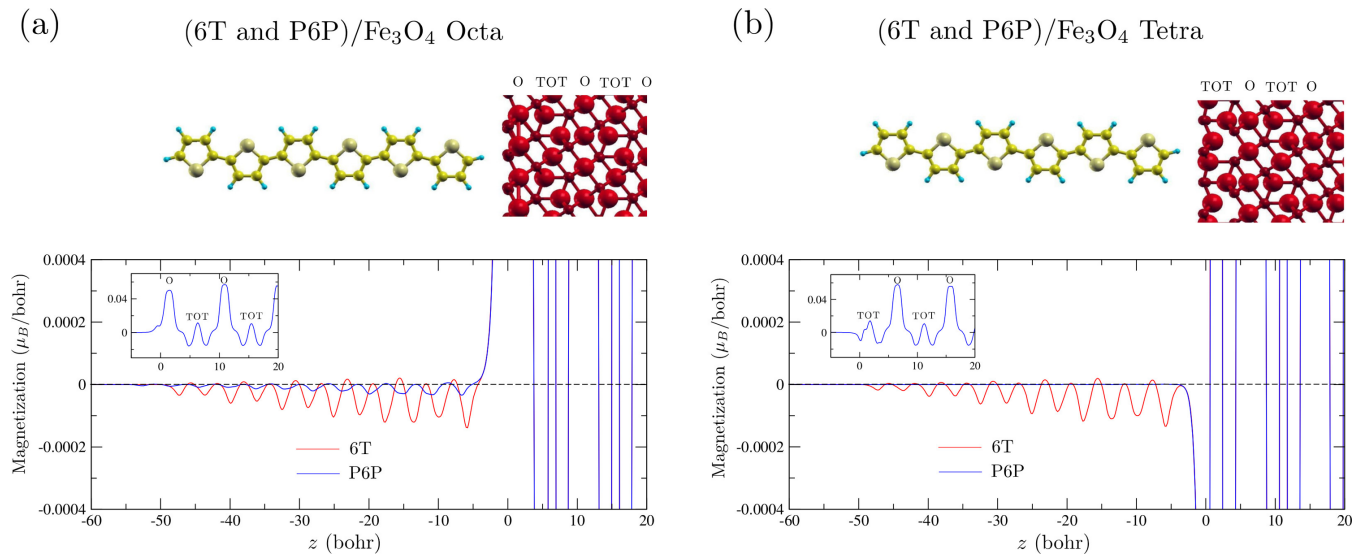

FIG. 9. DFT results for hybrid π-conjugated molecule/Fe_3O_4 interfaces of different terminations. (a) 6T (and P6P) at Fe_3O_4 terminated by octa. (b) 6T (and P6P) at Fe_3O_4 terminated by tetra. Upper panels: 6T/Fe_3O_4 adsorption configurations (similar for P6P molecule); Fe layers in octa positions are labeled as O (the other Fe atoms are in tetra positions). Lower panels: in-plane averaged spin moment as a function of z (perpendicular to the Fe_3O_4 surface) for 6T/Fe_3O_4 (red) and P6P/Fe_3O_4 (blue). Insets: the same plot, but at a larger scale.

molecules (compared to 6T): (i) deeper position of the HOMO orbital with respect to the Fermi level and (ii) breaking of conjugation between phenyl cycles in P6P molecular wires. Control and tuning of these parameters, for example by a gating, may therefore be considered as a possible way for driving the resulting magnetic coupling.

Thus, we show that it is possible to modify the strength of the magnetic exchange coupling in hybrid heterojunctions via organic spacer layers. We can suppose that manipulating the molecules/magnetic surface exchange interaction should allow one to tune the spin current at the interface (e.g., the sign of the magnetoresistance) and lead to using such current in molecule-based spintronic devices.

ACKNOWLEDGMENT

This work was supported by the RTRA on the Saclay plateau under the project "HeteroSpinMol."

[1] C. Chappert, A. Fert, and F. Nguyen Van Dau, Nat. Mater. **6**, 813 (2007).
[2] P. Grünberg, R. Schreiber, Y. Pang, M. B. Brodsky, and H. Sowers, Phys. Rev. Lett. **57**, 2442 (1986).
[3] S. S. P. Parkin, N. More, and K. P. Roche, Phys. Rev. Lett. **64**, 2304 (1990).
[4] S. Yuasa, T. Nagahama, A. Fukushima, Y. Suzuki, and K. Ando, Nat. Mater. **3**, 868 (2004).
[5] J. Faure-Vincent, C. Tiusan, C. Bellouard, E. Popova, M. Hehn, F. Montaigne, and A. Schuhl, Phys. Rev. Lett. **89**, 107206 (2002).
[6] H.-C. Wu, S. K. Arora, O. N. Mryasov, and I. V. Shvets, Appl. Phys. Lett. **92**, 182502 (2008).
[7] J.-H. Chung, Y.-S. Song, T. Yoo, S. J. Chung, S. Lee, B. J. Kirby, X. Liu, and J. K. Furdyna, J. Appl. Phys. **110**, 013912 (2011).
[8] J. C. Slonczewski, Phys. Rev. B **39**, 6995 (1989).
[9] P. Bruno, Phys. Rev. B **52**, 411 (1995).
[10] P. Sankowski and P. Kacman, Phys. Rev. B **71**, 201303(R) (2005).
[11] H.-C. Wu, O. N. Mryasov, K. Radican, and I. V. Shvets, Appl. Phys. Lett. **94**, 262506 (2009).
[12] M. Y Zhuravlev, E. Y. Tsymbal, and A. V. Vedyayev, Phys. Rev. Lett. **94**, 026806 (2005).
[13] C. Blouzon, F. Ott, L. Tortech, D. Fichou, and J.-B. Moussy, Appl. Phys. Lett. **103**, 042417 (2013).
[14] Z.-H. Xiong, D. Wu, Z. V. Vardeny, and J. Shi, Nature (London) **427**, 821 (2004).
[15] V. A. Dediu, M. Murgia, F. C. Matacotta, C. Taliani, and S. Barbanera, Solid State Commun. **122**, 181 (2002).
[16] T. S. Santos, J. S. Lee, P. Migdal, I. C. Lekshmi, B. Satpati, and J. S. Moodera, Phys. Rev. Lett. **98**, 016601 (2007).
[17] J. H. Shim, K. V. Raman, Y. J. Park, T. S. Santos, G. X. Miao, B. Satpati, and J. S. Moodera, Phys. Rev. Lett. **100**, 226603 (2008).
[18] C. Barraud, P. Seneor, R. Mattana, S. Fusil, K. Bouzehouane, C. Deranlot, P. Graziosi, L. Hueso, I. Bergenti, V. Dediu, F. Petroff, and A. Fert, Nat. Phys. **6**, 615 (2010).
[19] M. Galbiati, C. Barraud, S. Tatay, K. Bouzehouane, C. Deranlot, E. Jacquet, A. Fert, P. Seneor, R. Mattana, and F. Petroff, Adv. Mater. **24**, 6429 (2012).
[20] M. Cinchetti, V. A. Dediu, and L. E. Hueso, Nat. Mater. **16**, 507 (2017).
[21] S. Sanvito, Nat. Phys. **6**, 562 (2010).
[22] J. S. Moodera, B. Koopmans, and P. M. Oppeneer, MRS Bull. **39**, 578 (2014).
[23] M. Gruber, F. Ibrahim, S. Boukari, H. Isshiki, L. Joly, M. Peter, M. Studniarek, V. Da Costa, H. Jabbar, V. Davesne, U. Halisdemir, J. Chen, J. Arabski, E. Otero, F. Choueikani, K. Chen, P. Ohresser, W. Wulfhekel, F. Scheurer, W. Weber, M. Alouani, E. Beaurepaire, and M. Bowen, Nat. Mater. **14**, 981 (2015).
[24] V. E. Campbell, M. Tonelli, I. Cimatti, J.-B. Moussy, L. Tortech, Y. J. Dappe, E. Rivière, R. Guillot, S. Delprat, R. Mattana, P. Seneor, P. Ohresser, F. Choueikani, E. Otero, F. Koprowiak, V. G. Chilkuri, N. Suaud, N. Guihery, A. Galtayries, F. Miserque, M.-A. Arrio, Ph. Sainctavit, and T. Mallah, Nat. Commun. **7**, 13646 (2016).
[25] K. V. Raman, A. M. Kamerbeek, A. Mukherjee, N. Atodiresei, T. K. Sen, P. Lazic, V. Caciuc, R. Michel, D. Stalke, S. K. Mandal, S. Blügel, M. Munzerberg, and J. S. Moodera, Nature (London) **493**, 509 (2013).
[26] Y. Liu, S. M. Watson, T. Lee, J. M. Gorham, H. E. Katz, J. A. Borchers, H. D. Fairbrother, and D. H. Reich, Phys. Rev. B **79**, 075312 (2009).
[27] B. Dieny, J.-P. Gavigan, and J.-P. Rebouillat, J. Phys.: Condens. Matter **2**, 187 (1990).
[28] See Supplemental Material at http://link.aps.org/supplemental/10.1103/PhysRevB.99.144405 for structural characterizations, chemical formulas, XPS analyses, and heterojunction x-ray measurements.
[29] A. V. Ramos, S. Matzen, J.-B. Moussy, F. Ott, and M. Viret, Phys. Rev. B **79**, 014401 (2009).
[30] V. A. Dediu, L. E. Huesco, I. Bergenti, and C. Taliani, Nat. Mater. **8**, 707 (2009).
[31] G. Reecht, F. Scheurer, V. Speisser, Y. J. Dappe, F. Mathevet, and G. Schull, Phys. Rev. Lett. **112**, 047403 (2014).
[32] A. Smogunov and Y. J. Dappe, Nano Lett. **15**, 3552 (2015).
[33] D. Fichou, J. Mater. Chem. **10**, 571 (2000).
[34] J. Noguès and I. K. Schuller, J. Magn. Magn. Mat. **192**, 203 (1999).
[35] M. Ziese, I. Vrejoiu, and D. Hesse, Appl. Phys. Lett. **97**, 052504 (2010).
[36] A. R. Rocha, V. M. Garcia Suarez, S. W. Bailey, C. J. Lambert, J. Ferrer, and S. Sanvito, Nat. Mater. **4**, 335 (2005).
[37] J. Noh, O. I. Osman, S. G. Aziz, P. Winget, and J.-L. Bredas, Chem. Matter. **27**, 5856 (2015).
[38] M. Strange, C. Rostgaard, H. Häkkinen, and K. S. Thygesen, Phys. Rev. B **83**, 115108 (2011).